nature photonics

ARTICLES

https://doi.org/10.1038/s41566-021-00851-6

High-precision digital terahertz phase manipulation within a multichannel field perturbation coding chip

Hongxin Zeng[1,5], Huajie Liang[1,2,5], Yaxin Zhang[1,2,5]✉, Lan Wang[1,2]✉, Shixiong Liang[3]✉, Sen Gong[1,2], Zheng Li[1], Ziqiang Yang[1,2], Xilin Zhang[1], Feng Lan[1,2], Zhihong Feng[3], Yubin Gong[1], Ziqiang Yang[1,2] and Daniel M. Mittleman[4]

Direct phase modulation is one of the most urgent and difficult issues in the terahertz research area. Here, we propose a new method employing a two-dimensional electron gas (2DEG) perturbation microstructure unit coupled to a transmission line to realize high-precision digital terahertz phase manipulation. We induce local perturbation resonances to manipulate the phase of guided terahertz waves. By controlling the electronic transport characteristics of the 2DEG using an external voltage, the strength of the perturbation can be manipulated, which affects the phase of the guided waves. This external control permits electronic manipulation of the phase of terahertz waves with high precision, as high as 2–5° in the frequency range 0.26–0.27 THz, with an average phase error of only 0.36°, corresponding to a timing error of only 4 fs. Critically, the average insertion loss is as low as 6.14 dB at 0.265 THz, with a low amplitude fluctuation of 0.5 dB, so the device offers near-ideal phase-only modulation.

Terahertz technology has potentially transformative applications in high-rate communication, biomedical imaging, holography, spectroscopy, radar and security[1–8]. In particular, as the demand for wireless bandwidth increases, wireless communication systems employing terahertz waves as carriers will provide ultra-high data rates, exceeding those of emerging 5G communication systems[4]. The demand for terahertz systems is driving the development of high-performance integrated terahertz devices[6]. As a result, the efficient and dynamic manipulation of the phase and amplitude of terahertz waves has become the subject of in-depth research, worldwide. One valuable strategy relies on dynamic metamaterials composed of a metamaterial and an active material. Approaches based on this idea have produced remarkable results in the dynamic manipulation of terahertz amplitude and phase[3,9–17]. Depending on the type of structure employed, various resonance modes have been studied, such as *LC* resonance[9], dipole resonance[16] and Fano resonance[11]. Since the first work to manipulate the phase of a terahertz wave with a combination of metamaterials and doped semiconductors[18] in 2006, various dynamic or tunable metamaterials for terahertz phase manipulation have emerged[19–27]. Strategies for creating an active device to manipulate the phase of terahertz waves have relied on doped silicon[20], vanadium oxide[25], graphene[21,28], high-electron-mobility transistors (HEMTs)[26], liquid crystals[29] and other dynamic materials. However, because this modulation strategy generally relies on a resonant interaction, it entangles both amplitude and phase, and it is hard to modulate just one without also changing the other. Nearly all of these examples also exhibited a limited range of linearity and limited accuracy, making them unsuitable for applications requiring high-precision phase modulation. Finally, almost all of the earlier devices are designed to operate on a free-space quasi-optic terahertz beam, not a guided wave, limiting the overall efficiency and scale.

To overcome the above issues, the development of terahertz phase modulation requires a completely new approach. A strategy that employs on-chip terahertz waves, instead of free-space terahertz waves, may enable convenient integration. Meanwhile, Cui et al. have recently introduced the idea of an information metamaterial[30–36], as a special digital metamaterial, consisting of coding metamaterials digitalized as '0' or '1'. The binary codes produce different effects on electromagnetic waves by varying the electromagnetic characteristics of the metamaterial. In this way, digital metamaterials can be programmed to realize numerous functions, such as wavefront manipulation[35], imaging[32,33] and holography[37]. These works suggest that phase manipulation can be programmed with different coding sequences to achieve a precise degree of phase shifting at high rate, although, as with most earlier works on terahertz metamaterials, it has so far been limited to implementations that rely on quasi-optic coupling.

In this Article, we describe a multichannel field perturbation coding chip (MFPCC), which combines digitally controlled two-dimensional electron gas perturbation microstructure units (2DEG-PMUs) with an on-chip transmission line. In contrast to the more commonly employed approach for dynamic metamaterials, the 2DEG-PMU is not directly coupled to the entire terahertz wave in free space, but rather with a portion of the terahertz guided wave. This coupling forms a local resonance that perturbs the guided terahertz wave. By carefully engineering the bias-dependent frequency response of these resonant units, we ensure that the perturbation

[1]Sichuan Terahertz Communication Technology Engineering Research Center, School of Electronic Science and Engineering, University of Electronic Science and Technology of China, Chengdu, China. [2]Yangtze Delta Region Institute (Huzhou), University of Electronic Science and Technology of China, Huzhou, China. [3]National Key Laboratory of Application Specific Integrated Circuit, Hebei Semiconductor Research Institute, Shijiazhuang, China. [4]School of Engineering, Brown University, Providence, RI, USA. [5]These authors contributed equally: Hongxin Zeng, Huajie Liang, Yaxin Zhang. ✉e-mail: zhangyaxin@uestc.edu.cn; wanglan@std.uestc.edu.cn; wialliam@163.com

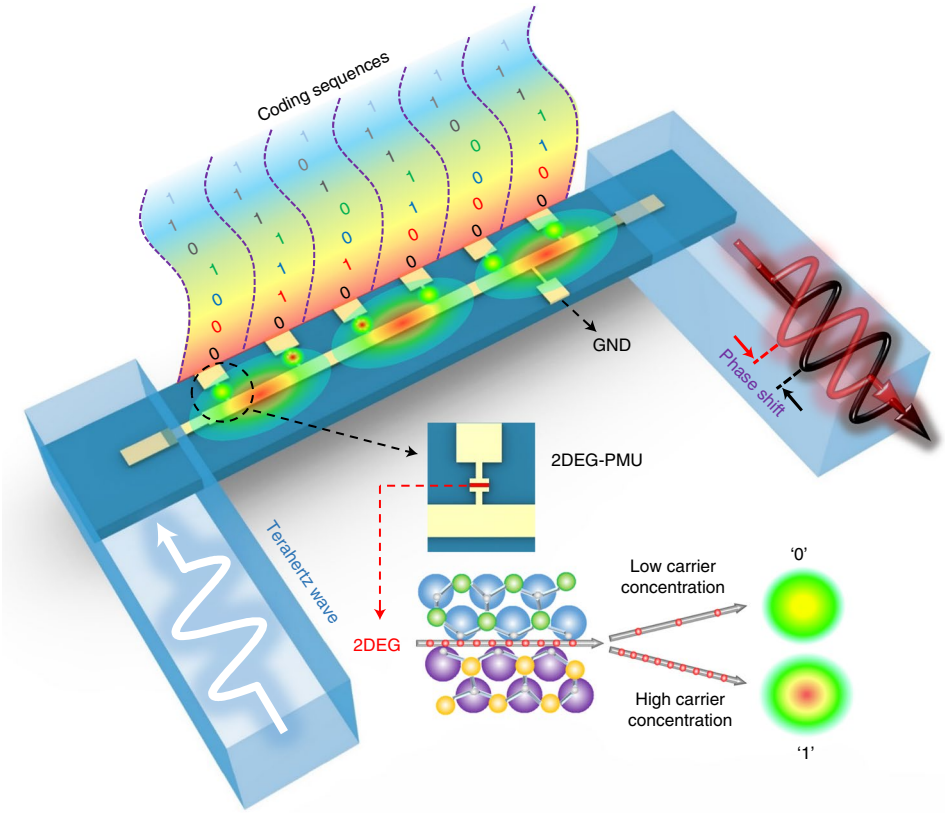

Fig. 1 | MFPCC architecture and its high-precision terahertz phase manipulation function. The on-chip microstrip line divides the surface of the substrate into two sides: one side contains 2DEG microstructures, and the other has a grounded metal pad. All of the metal layers are 1-μm-thick gold, fabricated on a 50-μm-thick SiC substrate. The width of the microstrip line is 54 μm. The 2DEG-PMUs consist of a section of microstrip line, a metal pad, a gapped thin metal line and two metal electrodes located on both sides of the gap. The 2DEG is nested in the gap, providing active properties to the device. By applying coding bias voltages to alter the electron transport characteristics of each 2DEG-PMU causing perturbations, we can combine various perturbation states to manipulate the terahertz phase.

of the terahertz wave is manifested as a phase shift, without significantly altering the amplitude. Moreover, digital coding of the perturbation intensity generated by an array of 2DEG-PMUs in series results in a nonlinear coupling that dramatically increases the diversity of the phase perturbations, enabling extremely precise control of the phase of the output terahertz signal.

The proposed MFPCC structure combines an on-chip microstrip transmission line with a series of 2DEG-PMUs (Fig. 1). The microstrip line divides the surface of the substrate into two sides: one side contains microstructures with integrated 2DEGs, and the other has a grounded metal pad. Each 2DEG-PMU consists of one metal pad, one gapped thin metal line and two metal electrodes located on both sides of the gap. The 2DEG, which uses the same manufacturing processes as conventional HEMT technologies[13], is nested in the gap, providing active properties to the device. When a terahertz wave is coupled to the input, it propagates along the main transmission line as a quasi-transverse electromagnetic (quasi-TEM or Goubau) mode[38], with its energy concentrated in the dielectric substrate. The electric field of this propagating terahertz wave can induce weak resonant modes in the nearby 2DEG-PMUs. A change in the electrical properties of the 2DEG caused by an applied bias voltage leads to a shift in the resonant response of the 2DEG-PMUs, which in turn affects the phase of the propagating terahertz guided wave.

By applying different bias voltages to the 2DEG, we can control the carrier concentration of the 2DEG to achieve conversion between the '0' (lower capacitance) and '1' (higher capacitance) states, realizing phase manipulation of the transmitting terahertz wave. (Details of the 0 state and 1 state resonance characteristics are described in Supplementary Sections I and II.) Cascading several 2DEG-PMUs in series (in Fig. 1, six 2DEG-PMUs are shown) has the effect of enhancing the overall dynamic range of the phase modulation.

There is an additional important effect of arranging multiple 2DEG-PMUs in series, as shown in Fig. 1. Each 2DEG-PMU along the microstrip line can individually exhibit the high and low capacitance states through different bias voltages, and these perturbations can superimpose on each other. However, these perturbations can cause mutual coupling, leading to a nonlinearity in the overall phase shift (Supplementary Section IV). As depicted in Fig. 1, each 2DEG-PMU of the array is coded with binary code sequences to convert it between the 0 and 1 states. Thus, various combinations of the states of all 2DEG-PMUs cause a precise and deterministic phase shift of the terahertz wave. However, due to the nonlinearity, the effects of individual 2DEG-PMUs do not simply add. We exploit this effect to achieve a higher dynamic range for the phase shift, with high precision from 2° to 5° in the frequency range from 0.26 to 0.27 THz. The average insertion loss at 0.265 THz is 6.14 dB, and the fluctuation of the amplitude of the output wave does not exceed 0.5 dB. Compared with earlier terahertz phase manipulation devices, our MFPCC demonstrates much higher-precision phase manipulation with low amplitude fluctuation. As a result of the integrated platform, it also has excellent scalability and compatibility for terahertz integrated systems.

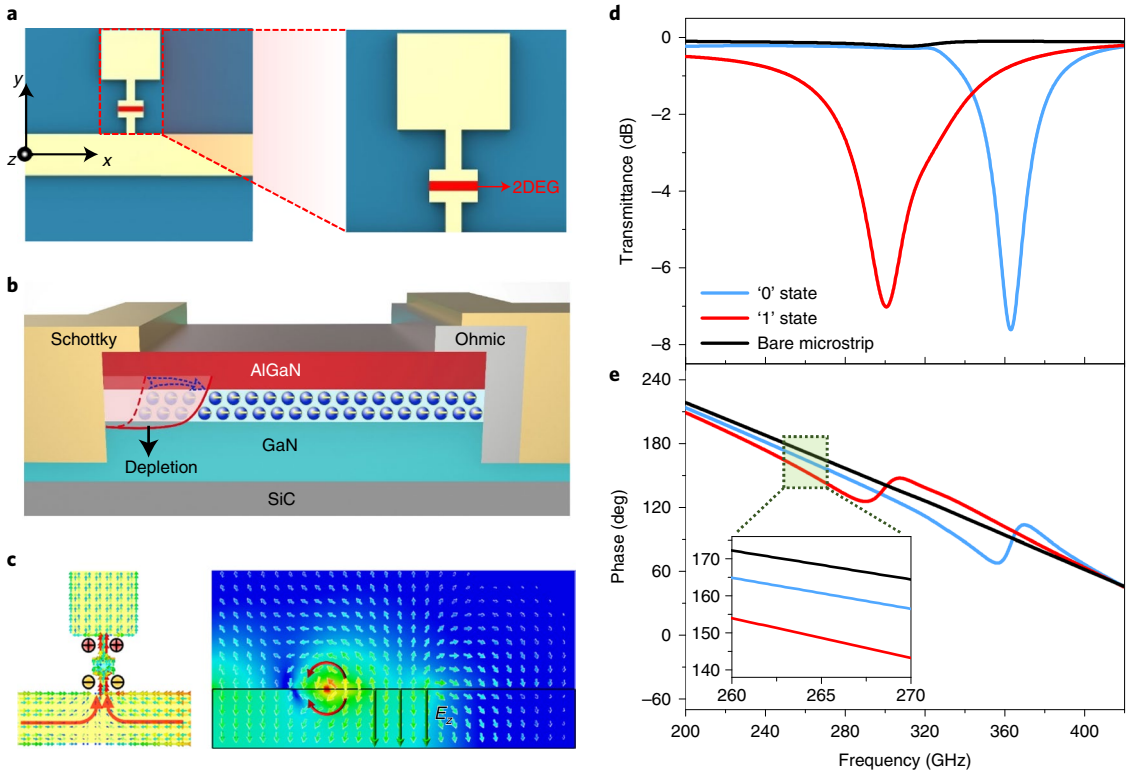

Fig. 2 | Perturbation and phase shift of a single 2DEG-PMU with 0 and 1 states. a, Structure of an individual 2DEG-PMU, where the blue is the SiC substrate, the yellow is the gold, and the red area in the centre is the 2DEG. The dimensions of the single 2DEG-PMU are provided in Supplementary Section II. **b**, The 2DEG structure in a 2DEG-PMU, in which the Schottky contact produces a depletion of the 2DEG layer (as indicated). **c**, Surface current and *y*–*z* cross-sectional electric field of the 2DEG-PMU. **d**, Simulated transmittance of a bare microstrip (black), a single 2DEG-PMU in the 0 state (blue) and a single 2DEG-PMU in the 1 state (red). **e**, Phase response of a bare microstrip (black), a single 2DEG-PMU in the 0 state (blue) and a single 2DEG-PMU in the 1 state (red). The enlarged part shows the phase of the 2DEG-PMU in the operation frequency band.

Results

Perturbation of the electromagnetic field by single 2DEG-PMUs. The structure of an individual 2DEG-PMU is shown in Fig. 2a, where the terahertz wave propagates in the *x* direction. The anode metal in the 2DEG structure is connected to the GaN film and AlGaN film, forming a Schottky contact that causes depletion of the 2DEG. In the depletion zone of the 2DEG, an equivalent capacitance is formed between the anode metal and the undepleted 2DEG. As shown in Fig. 2b, by varying the reverse bias on the anode of the 2DEG structure, we can change the width of the depletion region, thus varying the equivalent capacitance between the anode metal and the 2DEG. The higher the reverse bias voltage, the larger the width of depletion and the larger the equivalent capacitance. A detailed analysis of this process is given in Supplementary Sections I and II. To clarify the digital operation mode, we assume that a reverse bias voltage of 7 V represents a 0 (lower capacitance) state and a reverse bias voltage of 0 V represents a 1 (higher capacitance) state. Figure 2c shows the surface current and *y*–*z* cross-sectional electric field of the 2DEG-PMU. When the terahertz wave passes through the 2DEG-PMU, current flows from the microstrip line into the 2DEG structure, causing electrons to accumulate on the electrodes of the 2DEG structure and forming a local *LC* resonance.

We observe that the *LC* resonance produces an additional electric-field component E_z (Fig. 2c), which affects the original electric field of the quasi-TEM-mode guided wave in the substrate. This additional *z* component only slightly affects the original electric field of the guided wave, so the amplitude fluctuation is small. However, it has a more significant effect on the phase by changing the area of the electric field distribution in the cross-section. This causes a change in the relative equivalent permittivity of the microstrip line. The phase velocity thus changes, producing a deterministic phase shift. In our design, this phase shift is digital, controlled by the shift between the 0 state and the 1 state in the applied bias.

In Fig. 2d,e, we compare the transmittance and phase response of a bare microstrip line to that of a single 2DEG-PMU in the two digital operation states. In the case of the bare microstrip line without the 2DEG-PMU, the transmittance and phase are almost flat over the frequency band 0.2–0.45 THz. After introducing the 2DEG-PMU, an *LC* resonance appears, the resonance frequency of which is determined by both the geometric dimensions and the capacitance of the 2DEG. The frequency of this resonance changes from 0.363 THz to 0.3 THz on shifting from the 0 state to the 1 state. We also observe the expected phase jump at the resonance frequency, as shown in Fig. 2e. Of course, the large change of amplitude at the resonant frequency would result in low transmittance and large amplitude fluctuations, which is not conducive to high-efficiency and high-precision phase manipulation. Accordingly, we choose an operating frequency away from this resonance peak to obtain a high-precision phase shift without a large amplitude change. Moreover, in Supplementary Fig. 2d, the transmittance of the single 2DEG-PMU can be divided into two regions centred on the resonance frequency: one with frequency lower than the resonance frequency and the other with frequency higher than the resonance frequency. According to the characteristics of *LC* resonance, the lower frequency band is the capacitive region with phase lag and the higher frequency band is the inductive region with phase lead. As shown in Fig. 2e, the phase change induced by the 2DEG-PMU at frequencies below the resonance

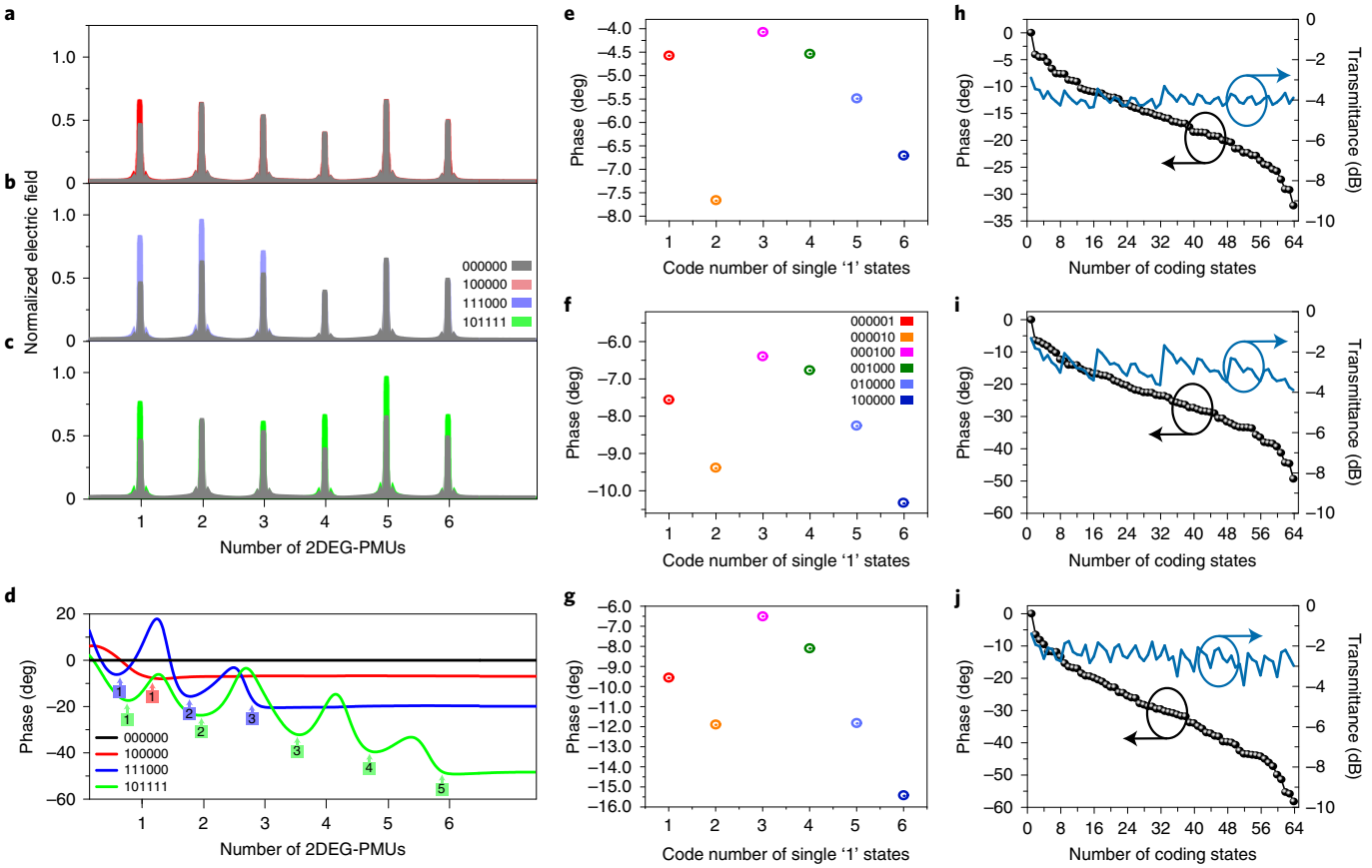

Fig. 3 | Simulation results of electric-field perturbation and phase manipulation of the MFPCC. a–c, Electric-field distribution of perturbation on the MFPCC encoded with '000000' (grey) and '100000' (red, **a**), '111000' (blue, **b**) and '101111' (green, **c**). **d**, Phase perturbations on the MFPCC encoded with '000000' (black), '100000' (red), '111000' (blue) and '101111' (green), with more perturbations corresponding to more phase shifts. **e–g**, For the case of a single '1' state, the phase shifts of different coding sequences at 0.26 THz (**e**), 0.265 THz (**f**) and 0.27 THz (**g**). **h–j**, Continuous phase shift and transmittance of the 64 coding states from coding sequence '000000' to '111111' at 0.26 THz (**h**), 0.265 THz (**i**) and 0.27 THz (**j**).

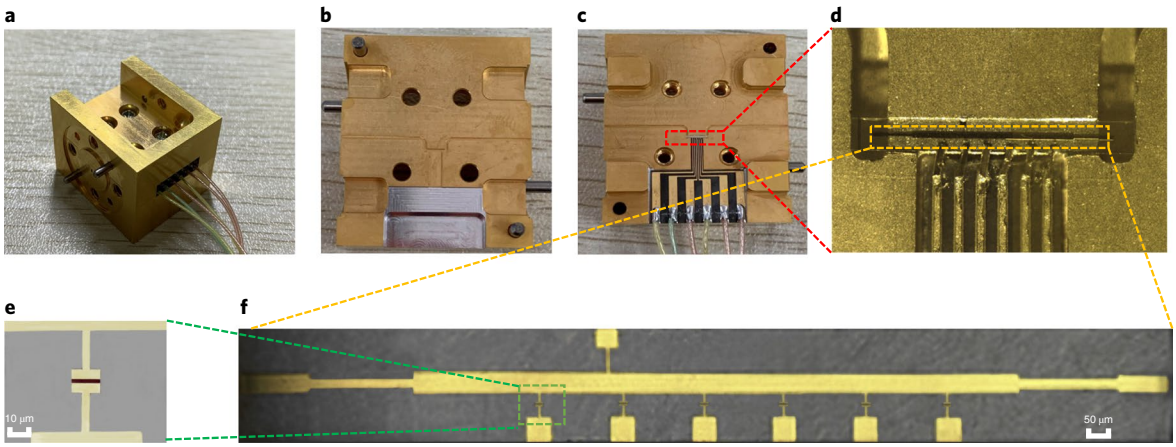

Fig. 4 | Photographs of the MFPCC and assembled test cavity. a–d, Photographic image of the fabricated test cavity containing the MFPCC. The test cavity (**a**) is composed of an upper cavity (**b**) and a lower cavity (**c**). **d**, The lower cavity is used to hold the MFPCC and the layout of the feeding circuit. **e**, Optical micrograph of a 2DEG-PMU. **f**, Optical micrograph of the MFPCC.

(capacitive region) is always negative, that is, smaller than that of the bare microstrip line, while just the opposite is true at frequencies above the resonance (inductive region). Because the 2DEG structure exploits capacitive tuning characteristics rather than inductive tuning characteristics, it possesses better phase manipulation performance in the capacitive region (below the resonance) than in the inductive region. Therefore, we choose an operating frequency range of 0.26–0.27 THz, below the resonant peak. We find that a phase shift of ~10° is obtained when the 2DEG-PMU shifts from the 0 state to the 1 state in the operating frequency band.

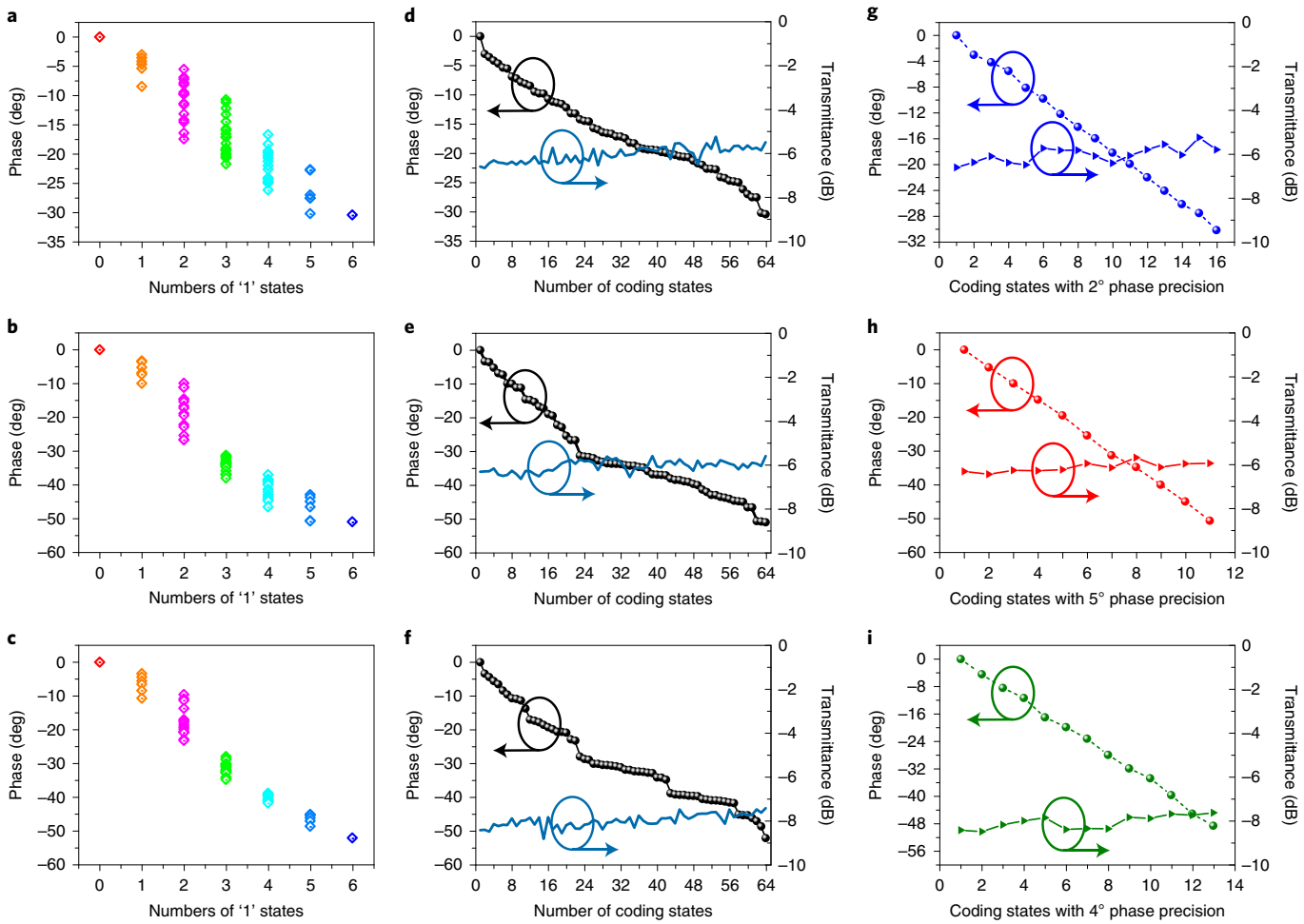

Fig. 5 | Experimental measurement results of MFPCC phase manipulation and transmittance. a–c, Phase shift as a function of the number of 1 states at 0.26 THz (**a**), 0.265 THz (**b**) and 0.27 THz (**c**). **d–f**, Phase shift and transmittance of the 64 coding states from coding sequence '000000' to '111111' at 0.26 THz (**d**), 0.265 THz (**e**) and 0.27 THz (**f**). **g–i**, High-precision and selected phase manipulation characteristics, with a precision of 2° at 0.26 THz (**g**), 5° at 0.265 THz (**h**) and 4° at 0.27 THz (**i**).

High-precision phase manipulation of the MFPCC. The above analysis indicates that the phase manipulation can be realized by varying the bias voltage applied to the 2DEG-PMU to tune a local *LC* resonance. We now consider the effect of having multiple 2DEG-PMUs in parallel along the microstrip line. Each 2DEG-PMU can be independently addressed and placed in either the 0 or the 1 state. This offers a great deal of flexibility in determining the state of the entire device.

As a demonstration, we consider a 2DEG coding chip containing six 2DEG-PMUs with a total of 64 coding states (Fig. 1). The state with code '000000' is set to the initial state as a reference. Figure 3a–c depicts the electric-field distributions of each 2DEG-PMU under three representative coding sequences: '100000', '111000' and '101111'. Here, all values of the local resonant electric-field intensity have been normalized by an arbitrary preset value. Under coding sequence '100000', the change in the state of the first 2DEG-PMU from the '000000' reference leads to a slight electric-field intensity enhancement in this first element, while the electric-field intensities of the other five 2DEG-PMUs remain the same as the initial state (Fig. 3a). Similarly, coding sequence '111000' produces electric-field intensity variations of the first, second and third 2DEG-PMUs, while the last three 2DEG-PMUs remain unchanged. In the case of coding sequence '101111', the electric field of the second 2DEG-PMU is the same as that of the initial state, while the other five 2DEG-PMUs have different values.

The surprising aspect of this analysis lies in the amplitudes of the changes in the electric-field intensities at the switched elements. For example, even though the first 2DEG-PMU is switched to the 1 state in all three examples, the resulting electric-field intensities at that element differ in all three cases. This result indicates that different coding sequences can lead to various electric-field intensity distributions due to the mutual coupling of the 2DEG-PMUs. As shown in Fig. 3d, the phase perturbations in the propagation process under the four example coding sequences are quite distinct. The figure shows that the three curves have one, three and five perturbations, respectively, which correspond to '1', '3' and '5' of the 1 states in the coding sequence. At the same time, the magnitude of the phase perturbation arising from the first 2DEG-PMU is different in the three coding sequences, even though the voltage on that element is the same in all three cases. This is a manifestation of the nonlinear interaction within the array of 2DEG-PMUs.

As another illustration, Fig. 3e–g shows the phase shifts for three different input frequencies resulting from a single 1 state, with coding sequences of '000001', '000010', '000100', '001000', '010000' and '100000', respectively. Obviously, if the device performance was purely governed by linear superposition, these six states would all

produce precisely the same output phase shift. Yet, we clearly see that the six coding sequences produce different output phase shifts.

We can make use of a transfer matrix method to accurately describe this nonlinear coupling[39]. Different coding sequences mean different orderings of the relevant transfer matrices, so the multiplication results change for different coding sequences, resulting in a nonlinear superposition of the phase shifts. Details of the coding phase shift theory for the multichannel field perturbation coding chip are provided in Supplementary Section IV.

We exploit this nonlinear superposition to obtain a wider diversity of phase shifts, thereby dramatically enhancing the precision of the achievable phase shift. Because the net output phase is not merely the sum of the fixed phase shifts from each of the six digital elements, the degeneracy of states with equal numbers of 1 states is lifted. The array device thus offers a much more plentiful selection of different phase shifts, similar to a coding phase database. We can determine all of these achievable phase shifts for each terahertz frequency to assemble this database. The simulated results of this database are shown in Fig. 3h–j for the multichannel field perturbation coding chip (MFPCC) illustrated in Fig. 1. At 0.26 THz, the continuous phase shift has a maximum of 35°, with an average insertion loss of 3.9 dB and amplitude fluctuation of 1 dB. At 0.265 THz, we can realize a continuous phase shift with a maximum phase shift of 50°. The minimum and maximum insertion losses of the chip are 1.3 dB and 3.6 dB, respectively. At 0.27 THz, the phase shift can reach 60°, again with a relatively low fluctuation of the insertion loss. We find that different working frequencies have their own phase distribution relation, while the insertion loss and amplitude fluctuation are always relatively low for all frequencies.

Experimental results of the MFPCC. Based on the analysis and simulation discussed above, we manufactured devices following the processing steps described in Supplementary Section V. The manufactured six-element MFPCC is shown in Fig. 4e,f. This device was packaged in a metallic cavity composed of an input/output hollow metallic rectangular waveguide, a chip loading area and a control circuit, as shown in Fig. 4a–d.

The control circuit is based on the Rogers 5880 (a type of printed circuit board of Rogers Corporation), which provides the coding external bias voltage input. Each 2DEG-PMU is connected to the pads on the Rogers 5880 by gold bond wires, which allows the external coding control voltage to be loaded on the 2DEG-PMU to realize digital coding phase manipulation.

The phase manipulation process can be described as three phases. In the first phase, after a terahertz wave is coupled to the rectangular waveguide, the *E*-plane waveguide-microstrip probe can couple the terahertz wave from the rectangular waveguide to the microstrip line. In the second phase, the terahertz wave propagates through the region coupled to 2DEG-PMUs while the external coding voltages are loaded, and a phase shift is induced. In the last phase, the terahertz wave is coupled to the rectangular waveguide and output to the terahertz detector. A vector network analyser is utilized to test the packaged device.

The results of the experiment are shown in Fig. 5. Figure 5a–c shows the relation between the number of 1 states and the phase shift of the 2DEG-PMUs at 0.26 THz, 0.265 THz and 0.27 THz, respectively. The phase shift increases with increasing number of 1 states, consistent with the simulations. Figure 5d–f shows the phase shift and insertion loss for all 64 possible coding sequences at 0.26 THz, 0.265 THz and 0.27 THz, respectively. At 0.26 THz, a total phase shift of over 30° with insertion loss of 5.3 dB (min) and 6.7 dB (max) can be achieved. In the same way, at 0.265 THz, we can obtain a total phase shift of over 50°, and the minimum and maximum insertion loss is 5.6 dB and 6.6 dB, respectively. Moreover, at 0.27 THz, we realize a total phase shift of up to 55°. These results are all in excellent agreement with the simulations of Fig. 4. Furthermore, by applying the principle that different coding sequences correspond to different phase shifts, we can select appropriate coding sequences to design the desired performance of the chip. An example is shown in Fig. 5h, where the designed multichannel field perturbation coding chip possesses a high phase shift precision of 5° at 0.265 THz, the average phase shift error is only 0.35° and the average insertion loss is as low as 6.14 dB. We obtain similarly remarkable results at other frequencies (Fig. 5g,i). It should be noted that the high-precision phase shift manipulation can be obtained with a very small amplitude fluctuation. The blue lines corresponding to the amplitude are nearly flat, at all frequencies, and the fluctuation of amplitude at 0.265 THz is only 0.5 dB. The measurement data corresponding to each coding state are shown in Supplementary Section VI. To our knowledge, this is the first example of a high-precision phase shifter in the terahertz range in which the phase shift is almost completely decoupled from the amplitude modulation. The remarkably high phase shift precision, together with the low and nearly phase-independent insertion loss, make this MFPCC a promising candidate for terahertz phase modulation in many future applications.

In summary, based on exploiting the electronic transport characteristics of a 2DEG and coupling these resonant elements to a transmission line, we have designed a multichannel field perturbation coding chip that offers high-precision digital control of the phase of a propagating terahertz wave, almost completely decoupled from amplitude modulation effects. Both the simulation and experimental results show that phase manipulation with precision ranging from 2° to 5° can be obtained at frequencies in the range from 0.26 to 0.27 THz, with an average phase error of only 0.36° (that is, only 0.1% of an optical cycle). Because of the small *RC* time constant associated with switching the 2DEG-PMU elements, we expect that this modulator can operate at a high modulation rate (details of the modulation rate are described in Supplementary Section I). Moreover, a larger phase shift could be obtained. For example, on applying 17 2DEG-PMUs in simulation, a 180° phase shift with a high-precision phase shift within 5° as well as a relatively low insertion loss can be achieved (Supplementary Section IV). This approach to on-chip digital phase control thus has excellent scalability and compatibility for terahertz integrated systems.

Online content

Any methods, additional references, Nature Research reporting summaries, source data, extended data, supplementary information, acknowledgements, peer review information; details of author contributions and competing interests; and statements of data and code availability are available at https://doi.org/10.1038/s41566-021-00851-6.

Received: 14 October 2020; Accepted: 24 June 2021;
Published online: 9 August 2021

References

1. Siegel, P. H. Terahertz technology. *IEEE Trans. Microw. Theory Tech.* **50**, 910–928 (2002).
2. Federici, J. F. et al. THz imaging and sensing for security applications—explosives, weapons and drugs. *Semicond. Sci. Technol.* **20**, S266–S280 (2005).
3. Wang, L. et al. A review of THz modulators with dynamic tunable metasurfaces. *Nanomaterials* **9**, 965 (2019).
4. Chen, Z. et al. A survey on terahertz communications. *China Commun.* **16**, 1–35 (2019).
5. Zheludev, N. I. & Kivshar, Y. S. From metamaterials to metadevices. *Nat. Mater.* **11**, 917–924 (2012).
6. Sengupta, K., Nagatsuma, T. & Mittleman, D. M. Terahertz integrated electronic and hybrid electronic–photonic systems. *Nat. Electron.* **1**, 622–635 (2018).
7. Watts, C. M. et al. Terahertz compressive imaging with metamaterial spatial light modulators. *Nat. Photon.* **8**, 605–609 (2014).
8. Dhillon, S. S. et al. The 2017 terahertz science and technology roadmap. *J. Phys. D* **50**, 043001 (2017).
9. Chen, H. T. et al. Active terahertz metamaterial devices. *Nature* **444**, 597–600 (2006).

10. Chen, H. T., O'Hara, J. F., Azad, A. K. & Taylor, A. J. Manipulation of terahertz radiation using metamaterials. *Laser Photon. Rev.* **5**, 513–533 (2011).
11. Singh, R., Al-Naib, I. A. I., Koch, M. & Zhang, W. Sharp Fano resonances in THz metamaterials. *Opt. Express* **19**, 6312–6319 (2011).
12. Yao, Y. et al. Broad electrical tuning of graphene-loaded plasmonic antennas. *Nano Lett.* **13**, 1257–1264 (2013).
13. Zhang, Y. et al. Gbps terahertz external modulator based on a composite metamaterial with a double-channel heterostructure. *Nano Lett.* **15**, 3501–3506 (2015).
14. Jessop, D. S. et al. Graphene based plasmonic terahertz amplitude modulator operating above 100 MHz. *Appl. Phys. Lett.* **108**, 171101 (2016).
15. Kim, T. T. et al. Amplitude modulation of anomalously refracted terahertz waves with gated-graphene metasurfaces. *Adv. Opt. Mater.* **6**, 1700507 (2018).
16. Zhao, Y. et al. High-speed efficient terahertz modulation based on tunable collective–individual state conversion within an active 3 nm two-dimensional electron gas metasurface. *Nano Lett.* **19**, 7588–7597 (2019).
17. Karl, N. et al. An electrically driven terahertz metamaterial diffractive modulator with more than 20 dB of dynamic range. *Appl. Phys. Lett.* **104**, 091115 (2014).
18. Chen, H. T. et al. A metamaterial solid-state terahertz phase modulator. *Nat. Photon.* **3**, 148–151 (2009).
19. Manceau, J. M., Shen, N. H., Kafesaki, M., Soukoulis, C. M. & Tzortzakis, S. Dynamic response of metamaterials in the terahertz regime: blueshift tunability and broadband phase modulation. *Appl. Phys. Lett.* **96**, 021111 (2010).
20. Shen, N. H. et al. Optically implemented broadband blueshift switch in the terahertz regime. *Phys. Rev. Lett.* **106**, 037403 (2011).
21. Lee, S. H. et al. Switching terahertz waves with gate-controlled active graphene metamaterials. *Nat. Mater.* **11**, 936–941 (2012).
22. Urade, Y. et al. Dynamically Babinet-invertible metasurface: a capacitive-inductive reconfigurable filter for terahertz waves using vanadium-dioxide metal-insulator transition. *Opt. Express* **24**, 4405–4410 (2016).
23. Ji, Y.-Y., Fan, F., Chen, M., Yang, L. & Chang, S.-J. Terahertz artificial birefringence and tunable phase shifter based on dielectric metasurface with compound lattice. *Opt. Express* **25**, 11405–11413 (2017).
24. Zhou, Z., Wang, S., Yu, Y., Chen, Y. & Feng, L. High performance metamaterials-high electron mobility transistors integrated terahertz modulator. *Opt. Express* **25**, 17832–17840 (2017).
25. Zhao, Y. et al. Dynamic photoinduced controlling of the large phase shift of terahertz waves via vanadium dioxide coupling nanostructures. *ACS Photonics* **5**, 3040–3050 (2018).
26. Zhang, Y. et al. Large phase modulation of THz wave via an enhanced resonant active HEMT metasurface. *Nanophotonics* **8**, 153–170 (2018).
27. Hu, Y. et al. Ultrafast terahertz frequency and phase tuning by all-optical molecularization of metasurfaces. *Adv. Opt. Mater.* **7**, 1901050 (2019).
28. Kakenov, N., Ergoktas, M. S., Balci, O. & Kocabas, C. Graphene based terahertz phase modulators. *2D Mater* **5**, 035018 (2018).
29. Yang, C.-S. et al. Voltage-controlled liquid-crystal terahertz phase shifter with indium-tin-oxide nanowhiskers as transparent electrodes. *Opt. Lett.* **39**, 2511–2513 (2014).
30. Cui, T. J., Qi, M. Q., Wan, X., Zhao, J. & Cheng, Q. Coding metamaterials, digital metamaterials and programmable metamaterials. *Light: Sci. Appl.* **3**, e218 (2014).
31. Zhang, X. G. et al. An optically driven digital metasurface for programming electromagnetic functions. *Nat. Electron.* **3**, 165–171 (2020).
32. Li, L. et al. Machine-learning reprogrammable metasurface imager. *Nat. Commun.* **10**, 1082 (2019).
33. Li, L. et al. Intelligent metasurface imager and recognizer. *Light: Sci. Appl.* **8**, 97 (2019).
34. Fu, X., Yang, F., Liu, C., Wu, X. & Cui, T. J. Terahertz beam steering technologies: from phased arrays to field-programmable metasurfaces. *Adv. Opt. Mater.* **8**, 1900628 (2020).
35. Wan, X. et al. Multichannel direct transmissions of near-field information. *Light: Sci. Appl.* **8**, 60 (2019).
36. Zhao, J. et al. Programmable time-domain digital-coding metasurface for non-linear harmonic manipulation and new wireless communication systems. *Natl Sci. Rev.* **6**, 231–238 (2019).
37. Li, L. et al. Electromagnetic reprogrammable coding-metasurface holograms. *Nat. Commun.* **8**, 197 (2017).
38. Treizebré, A., Akalin, T. & Bocquet, B. Planar excitation of Goubau transmission lines for THz BioMEMS. *IEEE Microw. Wirel. Components Lett.* **15**, 886–888 (2005).
39. Jackson, J. D. *Classical Electrodynamics* 3rd edn (Wiley, 1999).

Methods

Fabrication of the 2DEG-PMUs. A prototype of the MFPCC was created in the following manner. In the first step, an epitaxial layer of AlGaN/GaN was grown on a SiC substrate by metal organic chemical vapour deposition (MOCVD). After removing oil stains and other impurities, such as metal ions, by the standard cleaning process for HEMTs, a process combining photolithography with excessive etching was used to etch away the zones that did not include the active regions (2DEG regions). Next, several processes, such as photolithography and electron-beam evaporation, were used to fabricate a complex metal layer of Ti/Al/Ni/Au on one side of the active regions. After a high-temperature rapid annealing process at 900 °C in nitrogen, the complex metal layer was lifted off to form an ohmic contact with the 2DEG for the negative electrodes. Next, a Ni/Au layer was fabricated on the other side of the active regions by precise electron-beam lithography, forming a Schottky contact for positive electrodes after the liftoff process. Finally, through photolithography, electron-beam evaporation and liftoff processes, a Ni/Au layer was fabricated for accurate connection of the ohmic and Schottky contacts, completing the structure of the 2DEG perturbation microstructure unit.

Measurement of the phase shift. Phase measurements of the terahertz wave reported in this Article relied on a terahertz vector network analyser (THz-VNA) for quantitative measurements. First, we connected our hollow metallic waveguide ports to the calibrated THZ-VNA. The 2DEG-PMUs were then independently fed with coding sequence biases via a Rogers feed circuit. The feed bias voltage was −7 V (0 state) or 0 V (1 state). Finally, the scattering parameters and phase shifts of each coding sequence were obtained from the THZ-VNA data.

Data availability

Data are available from the corresponding authors upon request. Source data are provided with this paper.

Acknowledgements

This work was supported by the National Natural Science Foundation of China under contract no. 61931006 (Y.Z.), the National Key Research and Development Program of China under contract no. 2018YFB1801503 (Y.Z.), the Fundamental Research Funds for the Central Universities no. ZYGX2020ZB011 (Y.Z.), the China Postdoctoral Science Foundation no. 2020M683285 (H.Z.), the National Natural Science Foundation of China under contracts 61921002 (Y.G.) and U20A20212 (Z.Y.) and the US National Science Foundation grant no. 1923733 (D.M.M.).

Author contributions

H.Z., H.L., Z.Y. and Y.Z. conceived the idea of the multichannel field perturbation coding chip. S.L. processed the 2DEG structure, carried out device assembly and constructed the experiment environment. S.G. and F.L. helped with the simulation. H.L. and L.W. performed experiments. L.W., Z.L. performed the data analyses. L.W., Z.L. and X.Z participated in the discussion of potential setups for the tests/measurements, and helped to draft the manuscript. Z.F. and Y.G. helped to improve the design of the metallic cavity and control circuit. D.M.M. contributed substantially to theoretical analysis and manuscript polishing.

Competing interests

The authors declare no competing interests.

Additional information

Supplementary information The online version contains supplementary material available at https://doi.org/10.1038/s41566-021-00851-6.

Correspondence and requests for materials should be addressed to Y.Z., L.W. or S.L.

Peer review information *Nature Photonics* thanks Juraj Darmo, Yanko Todorov and the other, anonymous, reviewer(s) for their contribution to the peer review of this work.

Reprints and permissions information is available at www.nature.com/reprints.